JPhys Photonics

TUTORIAL • OPEN ACCESS

A practical guide to digital micro-mirror devices (DMDs) for wavefront shaping

To cite this article: Sébastien M Popoff *et al* 2026 *J. Phys. Photonics* **8** 023002

IOP Publishing J. Phys. Photonics 8 (2026) 023002 https://doi.org/10.1088/2515-7647/ae60d5

Journal of Physics: Photonics

TUTORIAL

A practical guide to digital micro-mirror devices (DMDs) for wavefront shaping

OPEN ACCESS

RECEIVED
29 September 2025

REVISED
14 January 2026

ACCEPTED FOR PUBLICATION
15 April 2026

PUBLISHED
11 May 2026

Sébastien M Popoff[1,*], **Louis Malosse**[2,3], **Rodrigo Gutiérrez-Cuevas**[1], **Yaron Bromberg**[4], **Jean Commère**[2], **Marie Glanc**[2], **Raphaël Galicher**[2] **and Maxime W Matthès**[1]

[1] Institut Langevin, ESPCI Paris, PSL University, CNRS, Paris, France
[2] LIRA, Observatoire de Paris, Université PSL, CNRS, Université Paris Cité, Sorbonne Université, Paris, France
[3] ISMO, University Paris Saclay, CNRS, Orsay, France
[4] Racah Institute of Physics, The Hebrew University of Jerusalem, Jerusalem, Israel
[*] Author to whom any correspondence should be addressed.

E-mail: sebastien.popoff@espci.psl.eu, louis.malosse@universite-paris-saclay.fr, rodrigo.gutierrez-cuevas@espci.psl.eu, jean.commere@obspm.fr, marie.glanc@obspm.fr and raphael.galicher@obspm.fr

Keywords: wavefront shaping, DMD, spatial light modulator

Supplementary material for this article is available online

Abstract

Digital micromirror devices have gained popularity in wavefront shaping, offering a high frame rate alternative to liquid crystal spatial light modulators. They are relatively inexpensive, offer high resolution, are easy to operate, and a single device can be used in a broad optical bandwidth. However, some technical drawbacks must be considered to achieve optimal performance. These issues, often undocumented by manufacturers, mostly stem from the device's original design for video projection applications. Herein, we present a guide to characterize and mitigate these effects. Our focus is on providing simple and practical solutions that can be easily incorporated into a typical wavefront shaping setup.

1. Introduction

Since the advent of adaptive optics, various technologies have been employed to modulate the amplitude and/or phase of light. Early adaptive optics devices, utilized in fields like microscopy and astronomy, offer rapid modulation capable of compensating for the aberrations of optical systems in real-time. However, these devices are constrained by a limited number of actuators, restricting their utility in complex media where a large number of degrees of freedom is essential. Liquid crystal spatial light modulators (LC-SLMs), which allow for the control of light phase across typically more than a million pixels, have emerged as powerful tools for wavefront shaping in complex media since the seminal work of A. Mosk and I. Vellekoop in the mid-2000s [1]. Nonetheless, LC-SLMs are hampered by their slow response time, permitting only a modulation speed ranging from a few Hz to a few hundred Hz.

Digital micromirror devices (DMDs) have emerged as a technology bridging the gap between these two types of systems; they offer a large number of pixels (similar to LC-SLMs) and fast modulation speeds (typically up to several tens of kHz). Their high speed capabilities made them attractive for real-time applications, in particular for high-resolution imaging microscopy requiring fast scanning or illumination shaping [2, 3], biolithography [4], and optical tweezers [5]. However, DMDs are restricted to hardware binary amplitude modulation and are not optimized for coherent light applications. Utilizing DMDs for coherent control of light in complex media is therefore non-trivial and necessitates specific adaptations for efficient use.

To comprehend both the capabilities and limitations of DMD technology for coherent wavefront shaping, it is crucial to understand the device's operating principles and its original design intentions. Investigated and developed by Texas Instruments since the 1980s, DMDs gained prominence in the 1990s for video projection applications since the 1990s under the commercial name of digital light processing (DLP) [6, 7]. The technology enables high-resolution, high-speed, and high-contrast-ratio modulation

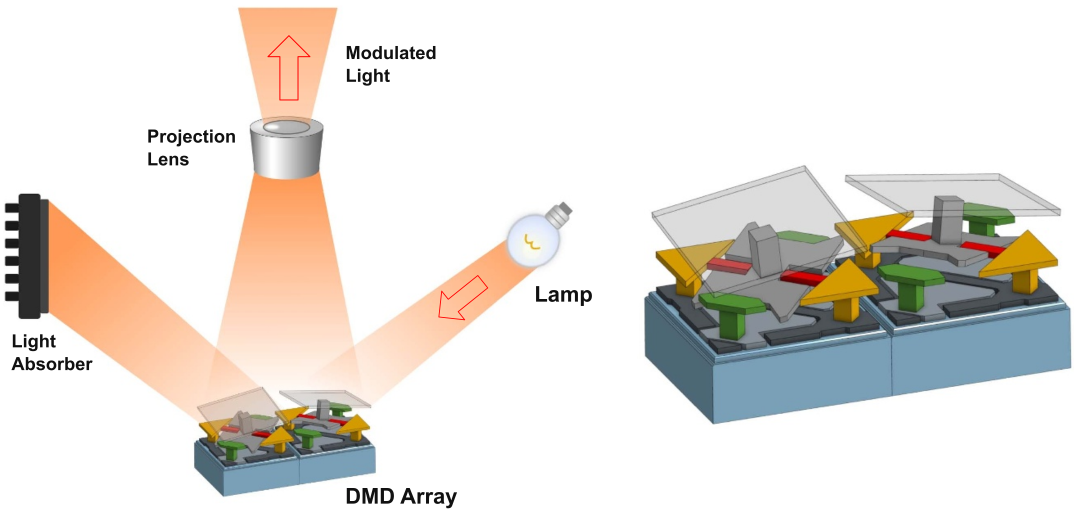

Figure 1. Principle of operation of a DMD in a digital projector. Left, incident light can be reflected towards the projection lens (state *on*), or onto a beam dump (state *off*). Right, zoom on the pixels. Image adapted from [17].

of light. DMDs operate by toggling the state of small mirrors between two distinct angles, denoted as $\pm\theta_{\mathrm{DMD}}$. The device is originally engineered for amplitude modulation in video projection applications. In this configuration, one mirror angle directs light into the projection lens, while the alternate angle results in the light path being blocked (see figure 1). Given that projectors utilize incoherent light and that the DMD plane is optically conjugated with the projection screen, aberrations within the DMD plane are generally not problematic. Similarly, phase fluctuations induced by temperature variations, as well as minor vibrations from the cooling hardware, are inconsequential in this context. The DMD is designed to produce binary on/off modulation, which is then leveraged to generate grayscale images via pulse-width modulation. Color modulation is accomplished through the use of a color wheel in conjunction with a bright white light source.

Third-party companies have developed kits tailored for research applications, which include a DMD, a control board, and a software interface. Specifically, Vialux devices [8] offer an FPGA board that enables high-speed modulation by allowing frames to be stored in the device's memory [9]. However, standard Texas Instruments video projector evaluation modules can also be repurposed into wavefront shaping devices [10], though at a compromised modulation speed. These systems can further be converted into phase or complex field modulators.

While other articles exist describing the various aspects of DMDs [10–13], this tutorial aims to provide a guide for easily setting up a DMD for wavefront shaping applications in complex media. In particular, we provide characterization and validation procedures that require minimal changes compared to typical wavefront shaping setups. More specifically, we place ourselves in a standard experiment where the goal is to shape the complex wavefront impinging on a complex medium and control or measure its output response. This is typically the case for a focusing experiment [1] or for measuring the transmission matrix of a complex medium [14]. In such works, complex modulation is usually achieved by encoding the optical phase into the spatial displacement of binary fringes displayed on the DMD, followed by filtering high spatial frequencies in the Fourier plane [15]. Such a configuration permits multi-level complex modulation, at the cost of a reduced spatial resolution. The implementation and performance of such systems are discussed in detail in a separate tutorial [16] and are not elaborated further here. For the remainder of this paper, it will be assumed that the DMD is used for complex modulation via such a method.

We first introduce the diffraction properties of a DMD and elaborate on how these could impact the system's efficiency. We also furnish a straightforward criterion for selecting the appropriate DMD parameters for a specified excitation wavelength. In the next section, we delve into the aberration impacts brought about by the non-flatness of the DMD surface. We demonstrate a simple process to characterize this effect and provide compensation solutions. In the third segment, we detail the influence of mechanical vibrations that are induced by the DMD's cooling system. Lastly, we discuss how the thermalization of the DMD chip can potentially result in variations to the DMD response over time.

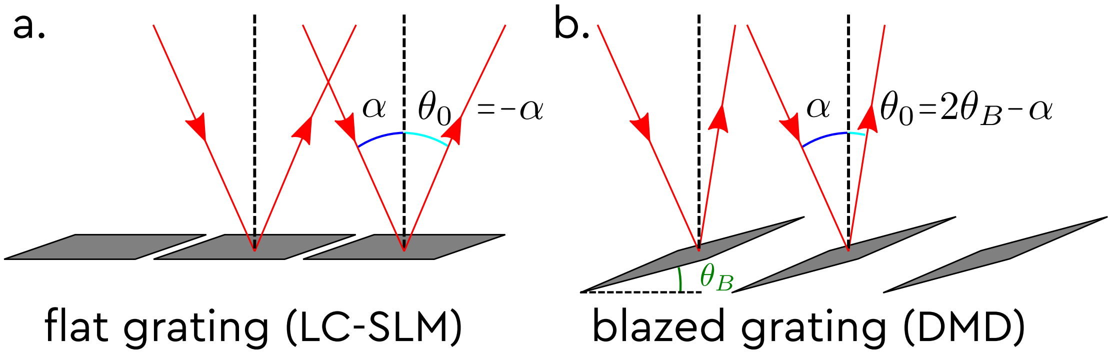

Figure 2. 1D grating geometry. Schematic representation of the geometry of two types of modulators: (a) the liquid crystal modulator, equivalent to a flat grating, and (b) the DMD geometry, equivalent to a blazed grating. α denotes the incident angle relative to the normal of the array plane, θ_0 refers to the angle of the zeroth diffraction order, and θ_B is the tilt angle of the mirrors.

2. Choosing the right DMD: diffraction effects

A significant distinction between liquid crystal modulators and DMDs lies in the geometry of the pixel surface: The pixels of the DMD are not flat, but are mirrors that can be tilted in two different positions around a rotation axis along the diagonal of the square shape of the pixels. This difference gives rise to diffraction effects that can adversely affect both modulation quality and diffraction efficiency, defined by the fraction of the incident optical power that is redistributed into a single diffraction order. The impact of these diffraction effects is highly dependent on several factors: the wavelength of illumination, the pixel pitch, and both the incident and outgoing angles. Therefore, in conjunction with selecting an appropriate anti-reflection coating, it is crucial to ensure that the pixel pitch is compatible with the specific configuration being used. Texas Instruments offers chips with a variety of pixel pitches d, ranging approximately from 5 to $\sim 25\,\mu$m [18].

2.1. A 1D model

To achieve a qualitative understanding of this issue, we consider a 1D array of pixels as illustrated in figure 2. Initially, let us assume that all pixels are in the same state and are illuminated by a plane wave originating from the far field. Under these conditions, the pixelated modulator essentially functions as a grating, with a period d that is equivalent to the pixel pitch. It is important to underscore that these modulators possess a hardware-limited filling fraction, typically around 90%. This translates to an effective active pixel size of $d' < d$.

Here we compare two types of gratings: flat gratings, corresponding to LC-SLMs, in which all pixels are in the same state; and blazed gratings, corresponding to DMDs, in which all pixels are tilted by the same angle. A grating gives rise to multiple diffraction orders, whose amplitudes are modulated by a global envelope. Importantly, these two effects can be decoupled. The diffraction order angles θ_p are determined by the grating periodicity, while the envelope, and in particular the position of its maximum $\theta_{\text{max}}^{\text{envelope}}$, is governed by the structure of a single pixel, which constitutes the unit cell of the grating.

2.1.1. Diffraction orders

In general, a grating gives rise to various diffraction orders with different intensities and angles θ_p, as dictated by the grating equation:

$$\sin(\theta_p) + \sin(\alpha) = p\lambda/d = p\sin(\theta_D), \tag{1}$$

where λ is the wavelength of the light, α is the incident angle, $\theta_D = \arcsin(\lambda/d)$ is the angle of the first diffraction order, and p is an integer value denoting the orders of diffraction. The intensity of the individual diffraction orders is influenced by the response of a single pixel, constituting the unit cell of the grating, and that is governed by d, d', and its rotation angle in the case of a DMD. While this regime is not always relevant, we can adopt the small-angle approximation to obtain a qualitative picture of the effect of the incident angle α on the diffraction orders. In this case, we have $\theta_p \approx p\lambda/d - \alpha$. Thus, changing the incident angle effectively rotates all diffraction orders by an angle $-\alpha$.

2.1.2. Position of the maximum of the envelope

The envelope of the diffracted field, which sets the amplitude of each diffraction order, is governed by the response of each unit cell, i.e. each pixel. In a flat grating excited at normal incidence, the envelope is peaked around the normal to the surface, i.e. $\theta_{\max}^{\text{envelope}} = 0$. In a blazed grating, the tilt angle θ_B introduces a linear phase ramp in the response of each individual pixel. A flat grating can be seen as a particular case with $\theta_B = 0$. The incidence angle α also adds a global phase slope. When the filling fraction approaches 100%, i.e. when $d \approx d'$, the cumulative effect leads to a shift of the envelope by an angle $2\theta_B - \alpha$. This results in a maximum of the envelope at

$$\theta_{\max}^{\text{envelope}} = 2\theta_B - \alpha \tag{2}$$

which reduces to $\theta_{\max}^{\text{envelope}} = -\alpha$ in the case of a flat grating. We detail the calculation of this effect in appendix A.

2.1.3. Blazed grating condition

In the case of a flat grating ($\theta_B = 0$), we see from equations (1) and (2) that the position of the first order is always aligned with the maximum of the envelope at the angle $-\alpha$, when the filling fraction is close to 1. In the general case $\theta_B \neq 0$, $\theta_{\max}^{\text{envelope}}$ does not, in general, coincide with any diffraction order [11, 13]. This leads to a redistribution of the energy of the incoming beam into multiple diffraction orders, resulting in a reduced diffraction efficiency as well as cross-talk between different pixel states, as studied in section 2.4.

The maximal diffraction efficiency is obtained when the maximum of the envelope matches one order of diffraction. This state is achieved when the conditions of the blazed grating equation are fulfilled [19], i.e. when there exist an integer p that satisfies:

$$\sin(2\theta_B - \alpha) + \sin(\alpha) = 2\sin(\theta_B)\cos(\theta_B - \alpha) = p\frac{\lambda}{d}. \tag{3}$$

In particular, in the Littrow configuration, i.e. for $\alpha = \theta_B$, we have $\theta_{\max}^{\text{envelope}} = \alpha$; the diffraction and incidence angles are identical. The optimal condition is then satisfied for $\sin(\theta_B) = p\lambda/(2d) = p\sin(\theta_D)/2$.

2.1.4. Example

We represent in figure 3 an example of a geometry for a 1D blazed grating and in figure 4 its angular response as well as the one corresponding to a flat grating with the same parameters. We take a 1D filling fraction of 95% (corresponding to a 2D filling fraction of $\approx$90%). For a flat grating, the zero-th order contains most of the intensity, the other orders being negligible in comparison. For the blazed grating example shown, we are in a situation close to the worst case scenario: two diffraction orders have a significant and comparable intensity, and other orders also have non-negligible contributions. In the optimal scenario, where the peak of the envelope corresponds to a diffraction order, it results in a single diffraction order carrying the majority of the energy. This state is achieved when the conditions of the blazed grating equation are fulfilled [19]:

2.2. The 2D case

2.2.1. Blazed grating condition

A DMD consists of a 2D array of micro-mirrors. In most DMDs, the rotation axis of the mirrors is aligned with the pixel diagonals. For convenience in the alignment and manipulation of the optical setup, it is preferable to work with incident and outgoing beams whose optical axes lie in the horizontal plane. A straightforward and common solution is to rotate the chip by 45° with respect to the horizontal plane, which makes the pixels' rotation axis vertical. This configuration is depicted in figure 5. We show in appendix B. that it leads to a new blazed grating equation that reads:

$$\sin(2\theta_B - \alpha) + \sin(\alpha) = 2\sin(\theta_B)\cos(\theta_B - \alpha) = p\frac{\sqrt{2}\lambda}{d}, \tag{4}$$

with p an integer. Note that this is what one would obtain using equation (3) for blazed grating with a pitch $d/\sqrt{2}$, or a 1D grating rotated by 45°. Those systems are not equivalent in the general case, but the grating condition in the 2D case is similar when considering an incident plane wave in the horizontal plane.

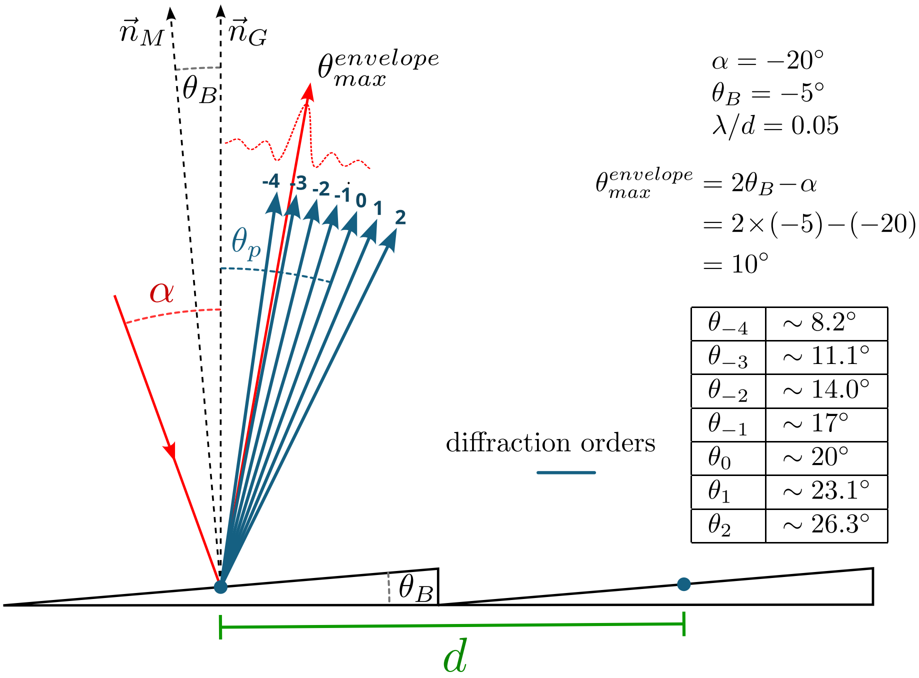

Figure 3. 1D grating example. All angles are defined with respect to the normal of the surface of the the grating, denoted by $\vec{n}_G$, and are taken as positive for clockwise rotations and negative for counter-clockwise rotations. The blazing angle θ_B is the angle between the normal to the micro-mirror $\vec{n}_M$ and $\vec{n}_G$. The angles of the diffraction orders θ_p are independent of θ_B, while the maximum of the envelope is at $\theta_{\text{max}}^{\text{envelope}} = 2\theta_B - \alpha$.

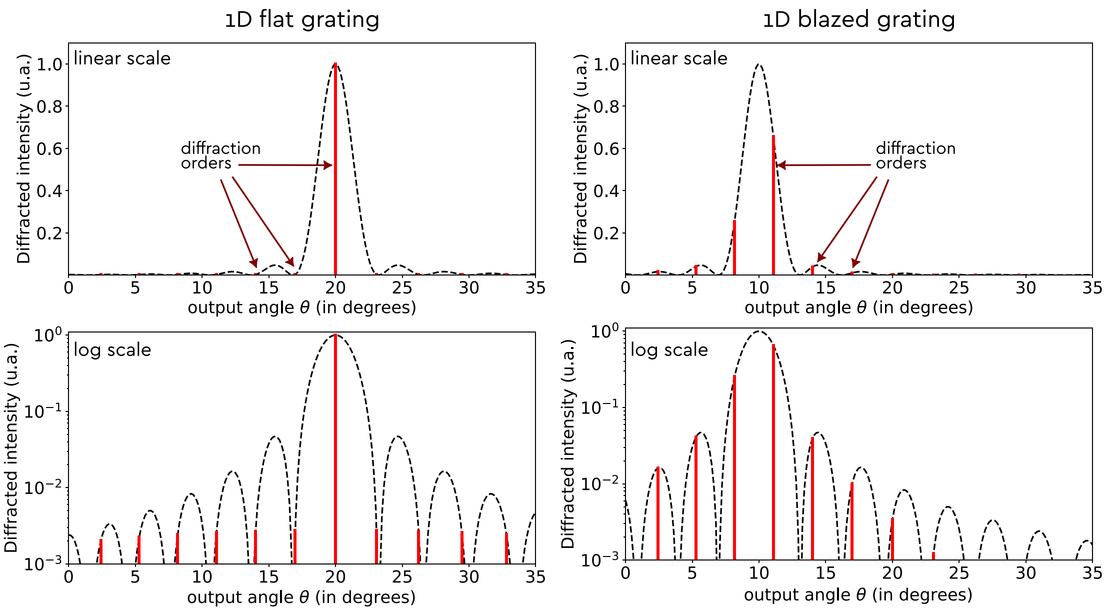

Figure 4. Flat grating vs blazed grating. Far field diffraction patterns for a 1D flat grating (left) and a 1D blazed grating (right) for an input angle of $\alpha = -20°$, a filling fraction of 95% (corresponding to a 2D filling fraction of $\approx 90\%$), a pixel tilt angle of $\theta_B = 5°$, and a wavelength to pixel pitch ratio $\lambda/d = 0.05$. Vertical lines represent the angles of the diffraction orders, peaked at θ_p which satisfy $\sin(\theta_p) + \sin(\alpha) = p\lambda/d$, and the black dashed curve represents the amplitude of the field which peaks at $\theta_{\text{max}}^{\text{envelope}} = 2\theta_B - \alpha$.

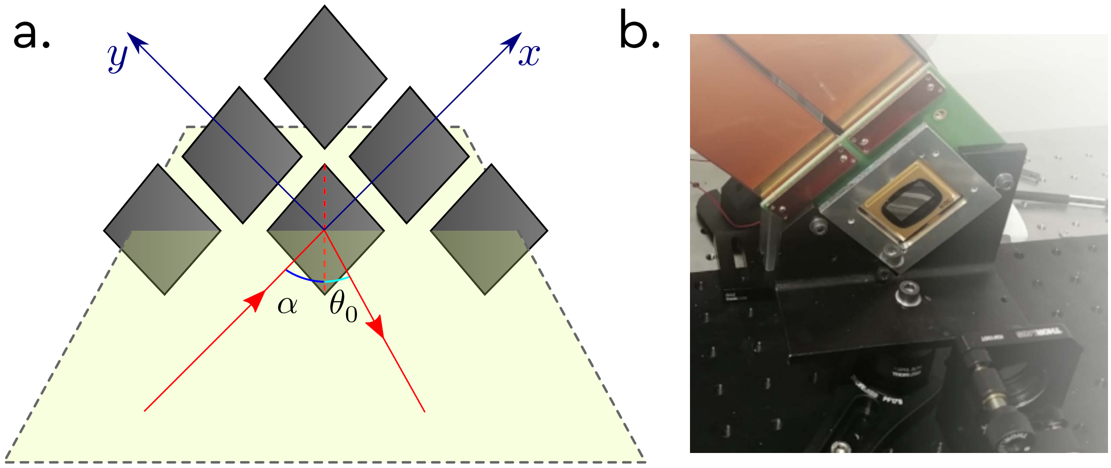

Figure 5. 2D grating geometry. (a) Schematic representation of the geometry of the DMD. The incident angle α and the reflection angle $\theta_{\max}^{\text{envelope}}$ (defined by the peak of the diffraction envelope) are situated within the horizontally plane, illustrated in yellow. (b) Photograph of the DMD chip oriented so that the rotation axis of the pixels is aligned vertically.

2.2.2. Blazed number

We can quantify how close we are to the ideal case, i.e. when satisfying the blazed equation, by defining a *blazed number* μ as introduced in [20]:

$$\mu = \left| 4\frac{d}{\sqrt{2}\lambda}\left[\sin\left(\theta_B\right)\cos\left(\theta_B - \alpha\right)\right] \mod 2 - 1 \right|, \tag{5}$$

where $\mod 2$ represents the modulo 2 operation. μ is maximal and equals 1 when the blazing equation is satisfied, i.e. when one order of diffraction contains most of the energy, corresponding to one diffraction order p being close to the maximum of the envelope ($\theta_p \approx \theta_{\max}^{\text{envelope}}$). μ is minimal in the worst-case scenario, i.e. when four diffraction orders have a significant and equal intensity. Note that, since the maximum of the envelope is no longer aligned with the zeroth order, corresponding to the specular reflection on the micro-mirrors, the value of the order p that aligns with the envelope peak when $\mu \approx 1$ can take any integer value, and depends on the DMD parameters and on the angle of incidence α.

2.2.3. Simulations

To demonstrate the effect, we first conduct a simulation of a DMD using Python (refer to tutorial and code in [20]) with two pixel pitches of $d = 7.6\,\boldsymbol{\mu}\mathbf{m}$ and $d = 10.8\,\mu$m, under a coherent excitation at $\lambda = 633$nm. Figure 6 shows the estimated blazed number μ as a function of the angle of incidence α in the horizontal plane, along with the far field diffraction pattern for two distinct incident angles. Figure 7 shows the blazed number as a function of both the incident angle and the wavelength for pixel pitches of $d = 7.6\,\mu$m and $d = 10.8\,\mu$m. It should be noted that the efficiency of diffraction, i.e. the fraction of the incident optical power that is diffracted into a given diffraction order relative to the incident power, can be altered by adjusting the angle of incidence α. However, its impact is relatively confined within an acceptable angular range that aligns with experimental limitations (i.e. for angles far from $\pm 90°$). Far-field patterns are centered around the maximum of the envelope for an output angle $2\theta_B - \alpha$ (marked by a red cross). We see that for small positive values of α, the pixel pitch of $d = 10.8\,\mu$m leads to a blazed number μ close to 1. It corresponds in the far field to having one bright order of diffraction close to the maximum of the envelope.

To illustrate the link between the blaze number and the efficiency of the diffraction setup, we compute the ratio of the energy in the brightest diffraction spot to the total diffracted energy for different values of the wavelength, with fixed values for the pixel pitch (7.6 μm) and incident angle (normal incidence). We simulate the DMD with no gap between the pixels (i.e. a filling fraction of 100%) and with 10 pixels in each direction, where all the mirrors of the pixels are in the same state. The results are shown in figure 8. We observe that the maxima (resp. minima) of the diffraction efficiency correspond to the maxima (resp. minima) of the blaze number. Note that the actual values of the minimum and maximum diffraction efficiency depend on the parameters of the DMD, such as pixel pitch, filling fraction, resolution, etc. In a practical situation, pixels are not all in the same state: the configuration is a mix of *on* and *off* states corresponding to angles $\pm\theta_B$. The diffraction efficiency then also depends on

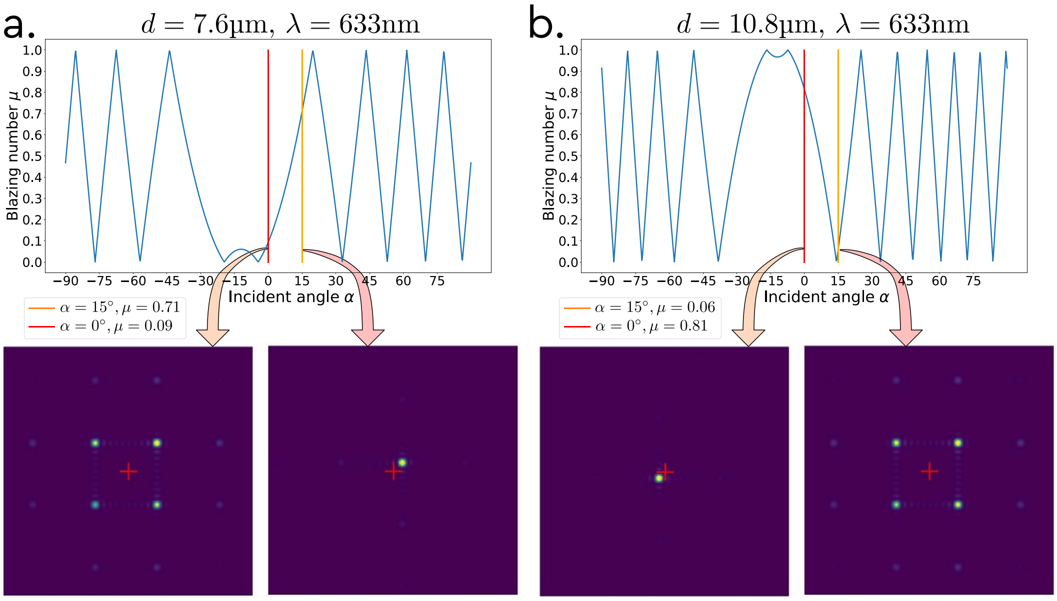

Figure 6. Blazed number and far-field diffraction patterns. Blazing number μ (equation (5)) as a function of the incident angle α (top) for a pixel pitch of $d = 7.6\,\mu$m (a.) and $d = 10.8\,\mu$m (b.). Corresponding far-field diffraction patterns (bottom) for two incident angles $\alpha = -15°$ and $\alpha = 0°$. The red cross indicates the maximum of the envelope $\theta_{max}^{envelope} = 2\theta_B - \alpha$ with $\theta_B = -12°$.

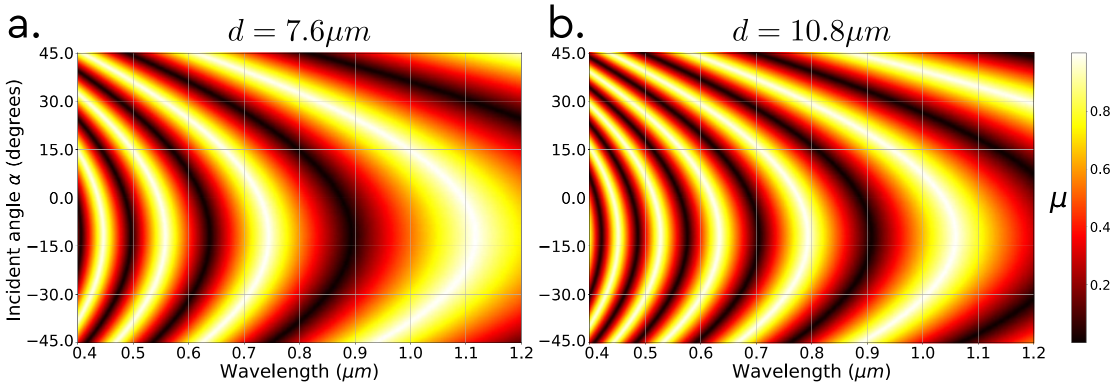

Figure 7. Blazed number as a function of the wavelength and the incident angle. Color map representation of the blazed number for a pixel pitch of $d = 7.6\,\mu$m (a.) and $d = 10.8\,\mu$m (b.) for $\theta_B = -12°$.

the modulation scheme and on the specific parameters used for the modulation. This topic is addressed in detail in a separate tutorial focusing on complex modulation using binary amplitude modulators [16].

2.3. Experimental measure of the optimal incident angles

We experimentally characterized a DLP9500 DMD with a pixel pitch of $d = 10.8\,\mu$m at $\lambda = 473$nm. The illumination geometry and DMD orientation are as presented in figure 5. The experimental setup, shown in figure 9, consists of an objective (L), a lens (L'), and a pinhole to produce a clean, collimated laser beam. A diaphragm is used to control the size of the beam incident on the DMD, and the reflected light is observed on a screen.

We then illuminate with a collimated monochromatic beam the DMD in its full-*on* (resp. full-*off*) state, corresponding to all pixels being rotated by an angle θ_B (resp. $-\theta_B$), with $\theta_B = 12°$. The light distribution across the diffraction orders can be assessed directly with the naked eye by placing a screen after reflection from the DMD. The DMD is mounted on a rotating plate with its axis of rotation orthogonal to the table, allowing variation of the angle α, as defined in figure 5. The reference angle ($\alpha = 0$) is determined by auto-collimating the incident beam with the DMD in its idle state ($\theta_B = 0$).

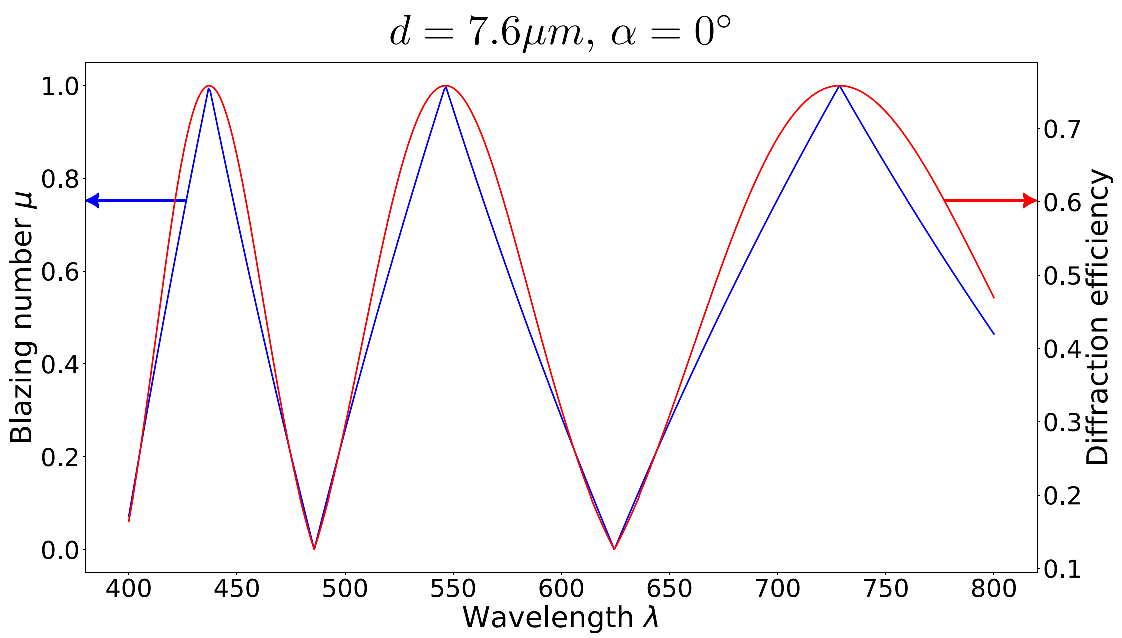

Figure 8. Blazed number vs diffraction efficiency. Plot of the blazed number and the diffraction efficiency for a normal incidence and a pixel pitch of 7.6 μm as a function of the wavelength. The diffraction efficiency is estimated by comparing the energy in a diffraction limited spot at the location of the brightest diffraction order to the total diffracted energy.

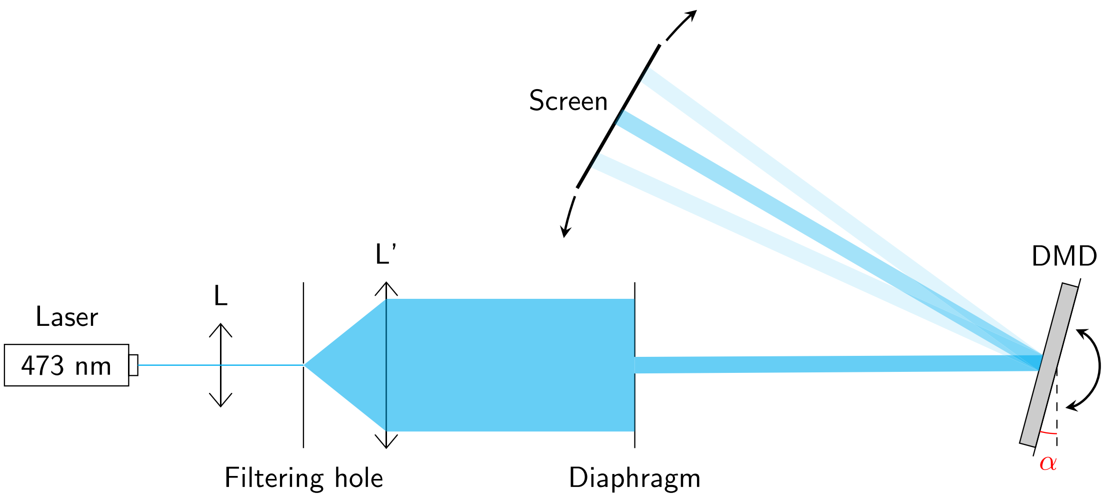

Figure 9. Blazed number maxima measurement set up. A laser beam is filtered and expanded using a telescope (objective *L* and lens *L*'). A diaphragm is used to adjust the beam diameter before it reflects off the DMD with all pixels in *on* (resp. *off*) state. A movable screen allows to see the brightest diffraction orders as the DMD is rotated.

The DMD is then rotated until the reflected light is almost entirely on a single diffraction order, with adjacent orders extinguished. The corresponding values of α are shown in figure 10 as red lines, illustrating a good correlation between the computed evolution of the blazed number μ (equation (5)) and the diffraction efficiency.

2.4. Modulation cross-talk

In practice, we place a pinhole or iris to select one order of diffraction, corresponding to the *on* state. Having a small value for the blaze number μ not only restricts the amount of light modulation due to the diminished diffraction efficiency, it also influences the modulation quality by inducing cross-talk between the two states of the DMD pixels. Until now, we have assumed that all the pixels are in the same state. In actual usage of the DMD, it becomes necessary to modulate the state of each pixel individually. When μ approaches zero, higher orders of diffraction still possess a significant intensity, as

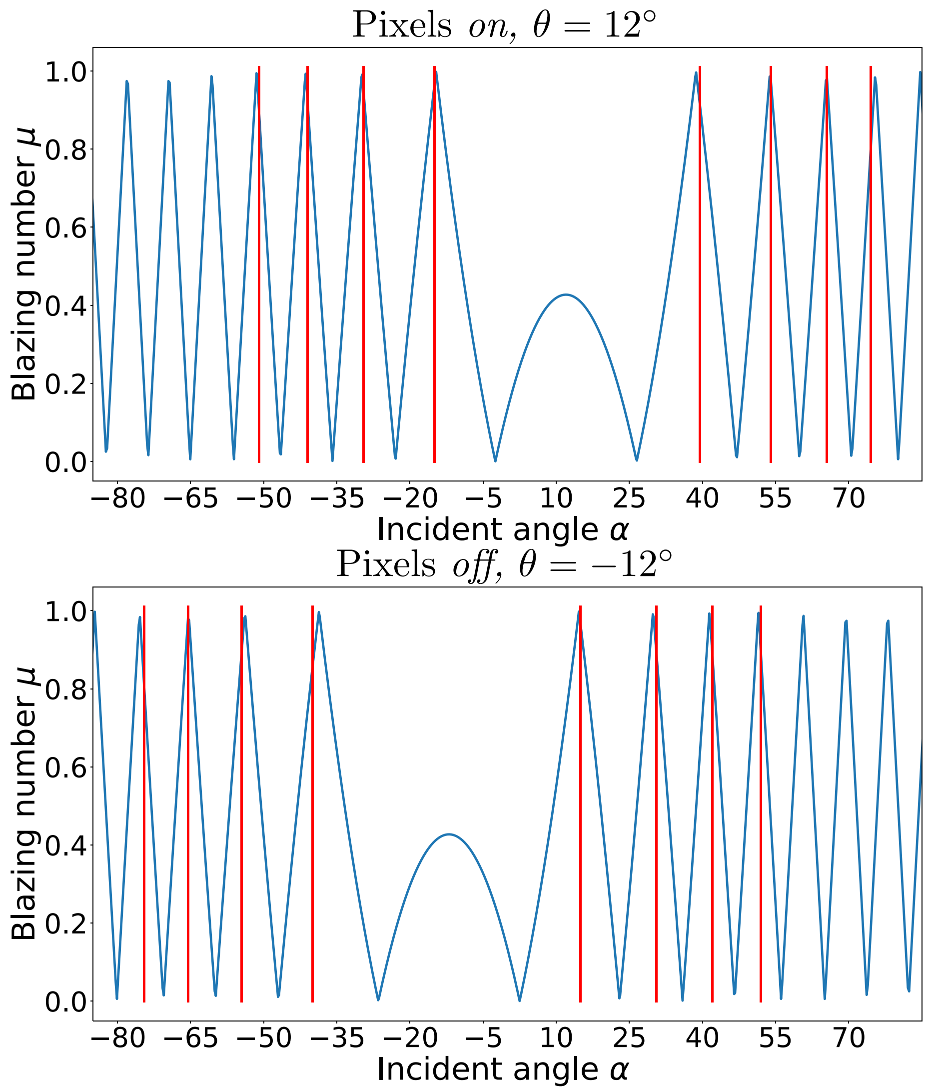

Figure 10. Optimal angles for diffraction efficiency, experiment vs predictions. Blazing number μ as a function of the incident angle α (top) for a pixel pitch of $d = 7.6\,\mu$m and $\lambda = 473$ nm, when all the pixels are *on*-state (resp. *off*-state), corresponding to a tilt angle $\theta = 12^\circ$ (resp. $\theta = -12^\circ$). Blue curves represent the predictions of equation (5) and red curves the experimentally measured angles for which the energy is maximal in one diffraction spot.

demonstrated in the 1D case in figure 4. One adverse implication is that pixels in the *off* state may contain orders of diffraction that are not blocked by the pinhole, and therefore, will contribute as an interference to the modulated wavefront. We show in figure 11 the normalized amplitude of the diffraction patterns corresponding to all the pixels in the *on* (blue curve) and *off* (orange curve) states for the same experimental conditions but with two different pixel pitches leading to situations close to the worst (a) and best (b) case scenarios. We observe the presence of a non-negligible contribution of the *off* state at the main diffraction order of the *on* state in the first case. While this contribution might appear weak, it does affect the quality of the modulation since the modulation scheme typically necessitates about half the pixels to be in the *off* state for phase modulation [15], and even more so for elaborate modulation schemes [16, 21].

2.5. Dispersion

DMDs are composed of metallic small mirrors, the response of which is minimally affected by wavelength changes. This is particularly advantageous for broadband applications requiring amplitude modulation and operating on a plane conjugated to the DMD's surface. This is the case for the originally intended application of video projection. However, for wavefront-shaping applications, it is typically required to select a specific diffraction order to achieve phase or complex modulation [15, 16]. Under such circumstances, the wavelength-dependency of the diffraction effect becomes important. The blazed number, denoted by μ (according to equation (5)), scales inversely with the wavelength. Figure 12 shows the blazed number μ as a function of the wavelength for two pixel pitches $d = 7.6\,\mu$m and $d = 10.8\,\mu$m,

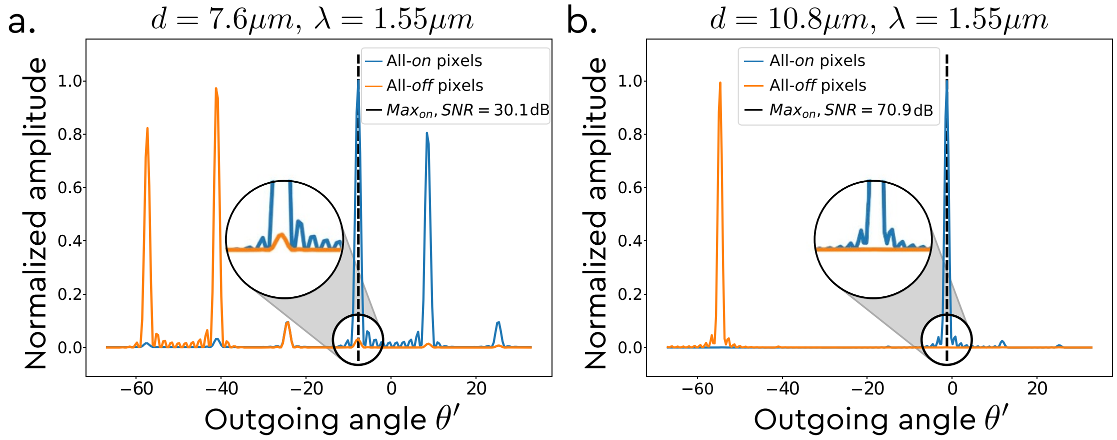

Figure 11. Cross-talk between *on* and *off* states. We show the computed normalized amplitude of the diffraction patterns corresponding to all the pixels in the *on* state (blue) and *off* state (orange) for two different pixel pitches, $d = 7.6\ \mu$m (a.) and $d = 10.8\ \mu$m (b.) with the same experimental conditions. In the first case, μ is close to 0, we observe a non-negligible contribution of the *off* state at the main diffraction order of the *on* state, thus creating unwanted cross-talk. In the second case, μ is close to 1, the contribution of the *off* state is negligible.

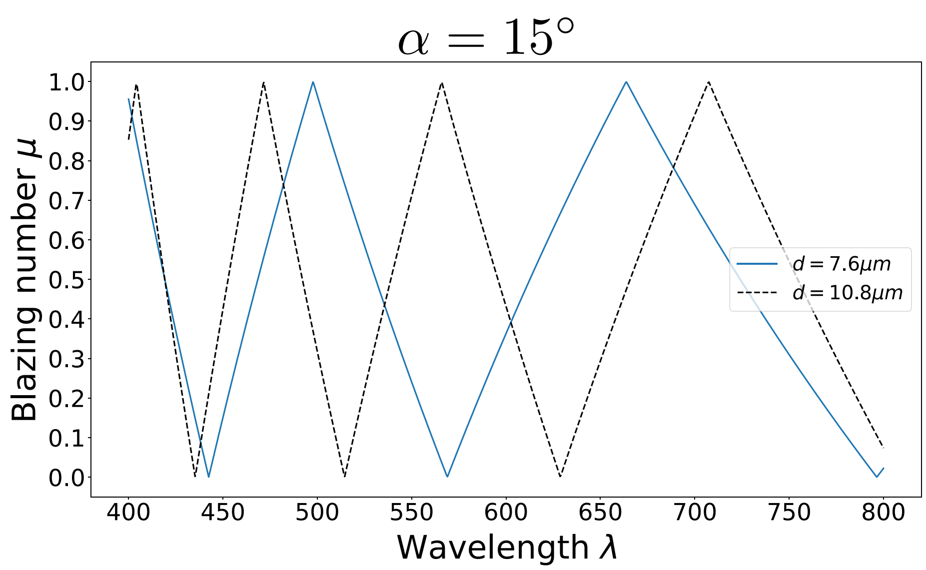

Figure 12. Dispersion of the diffraction effect. Blazing number μ (equation (5)) as a function of the incident wavelength for an incident angle $\alpha = 20°$ and a pixel pitch of $d = 7.6\ \mu$m (blue curve) and $d = 10.8\ \mu$m (dashed black curve).

with an incident angle of $\alpha = 20°$. Within the visible spectrum, μ fluctuates between 0 to 1 over a typical range of roughly 100 nm.

TL;DR:
DMDs act as blazed gratings. For a given operation wavelength, we need to find the right pixel pitch to have a good modulation quality and diffraction efficiency. It can be done by estimating the *blazed number* μ introduced in equation (5) or directly using our custom online tool [22].

2.6. Python code example

We provide in the paper repository [23] a Python code to simulate the diffraction effect of a DMD by computing the far field pattern for a set of realistic parameters. It provides a simple way to estimate the blazed number μ introduced in equation (5) to assess the quality of the modulation at the desired wavelength for a given pixel pitch. We also propose an online tool accessible at www.wavefrontshaping.net/post/id/49.

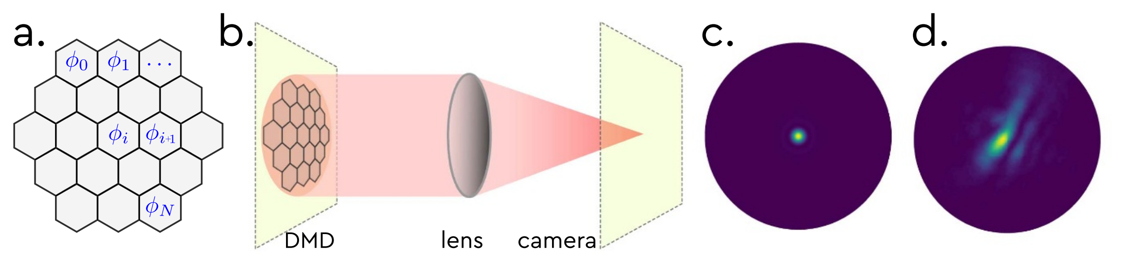

Figure 13. Setup for aberration correction. (a) A schematic representation of the DMD array divided into macropixels, of which the phase can be controlled. The precise shape of the macropixels and the area controlled are not crucial for the characterization of aberrations to be effective, provided that the spatial sampling is sufficient to capture the highest spatial frequencies of the aberrations. (b) A schematic representation of the setup employed to characterize the aberrations. A camera is used to image the far field on the DMD surface using a lens. (c) Shows the ideal intensity pattern corresponding to the numerical aperture of the illumination setup, i.e. its theoretical ideal PSF. (d) Show the actual recorded intensity pattern corresponding to a distorted PSF due to the DMD aberrations.

3. Characterizing aberration effects

3.1. Presentation of the problem

While only capable of providing hardware binary amplitude modulation, DMDs serve as a potent tool for wavefront shaping and sensing. These applications critically require characterization and correction of aberrations caused by the non-flatness of the DMD surface. For LC-SLMs, the manufacturer typically characterizes the surface's inhomogeneities within the plane of the modulator and provides a spatial phase profile of the introduced aberrations based on the operational wavelength. It is noteworthy that when utilized for intensity modulation on a plane conjugated to the DMD plane, as it is done in digital projectors, the system becomes insensitive to the aberrations caused by the DMD surface. Consequently, these effects are commonly overlooked and rarely documented in the information provided by the manufacturers. However, studies suggest that the residual stresses developed in the thin films during the manufacturing process of the DMDs induce non-negligible surface deformations [24–26].

3.2. Finding the correction pattern

In the literature, various methods have been proposed to characterize the phase pattern of the DMD aberrations in the plane of the modulator. Typically, this involves using a model for the aberrations, tweaking the parameters to align with the measurements [12, 26, 27]. An alternative approach entails direct measurement of the distorted wavefront, either employing a wavefront sensor such as a Shack-Hartmann [28], or via interferometry. While such methods yield accurate results, they necessitate adaptation to the particular setup conditions, and frequently require supplementary optical components, meticulous alignment, and custom software. Moreover, once the phase correction map has been obtained, it must then be aligned with the pixel array in order to implement the phase correction on the DMD and compensate for aberrations. In this section, we introduce a straightforward method for characterizing aberrations using a lens and a camera. The goal is to *in situ* compensate for the aberrations using a phase modulation scheme (Lee holograms), by iteratively optimizing the point spread function (PSF) at the focal plane of a lens. The resulting phase correction map is the conjugate of the one induced by the surface deformation of the DMD, and can subsequently be used to correct aberrations with any desired complex modulation scheme. This technique can be employed for any system that offers phase modulation, such as LC-SLMs or deformable mirrors.

We assume that the DMD is configured to deliver phase modulation [15, 16]. It is classically done using Lee holograms or similar approaches, where the optical phase is encoded in the local spatial displacement of a regular array of amplitude fringes displayed on the DMD. By filtering a single diffraction order, the resulting field retains only the phase modulation. Specific implementations and variants of such approaches are discussed in [16]. This implies that the modulator can be divided into N sections, which we designate as *macropixels*, where the phase can be controlled independently. We use a lens and a camera in its Fourier plane, illuminating the modulator with a collimated beam that extends over the entire area of the modulator intended for use. In scenarios where there are minimal or no aberrations, the intensity pattern observed would mimic the PSF of the lens, such as an Airy disk depicted in figure 13(c). However, in practice, we encounter a substantially distorted pattern, like the one represented in figure 13(d). A more detailed depiction of the setup for aberration characterization, in the context of a wavefront shaping application in complex media is presented in figure 14(a). In the case where the

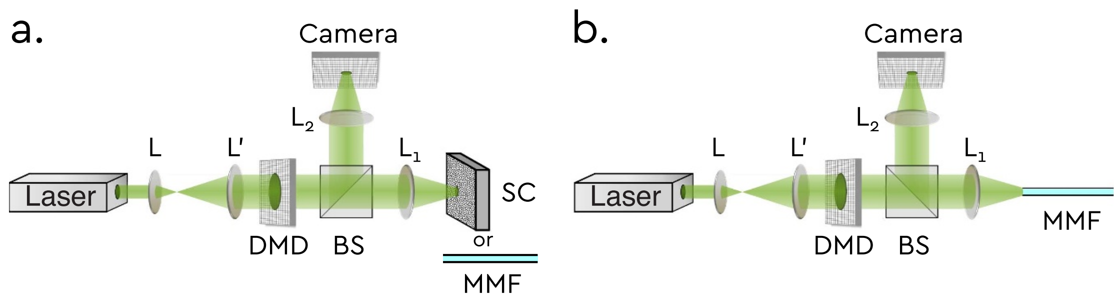

Figure 14. Detailed aberration characterization setup. (a) A laser beam is expanded and collimated using a telescope (lenses L and L'). The DMD is represented in transmission for simplicity. Light reflected from the DMD is focused by a lens L_1 onto the complex medium to study, namely a scattering medium (SC) or a multimode fiber (MMF). A beamsplitter is used to image the far field of the DMD onto a camera using a lens (L_2). The intensity pattern, up to a homothetic transformation, represent the input excitation on the medium which also corresponds to the PSF of the illumination setup. (b) In the case of a multimode fiber, one can take advantage of the reflection of the input facet to directly image the intensity pattern of the input plane.

medium is a multimode fiber, one could leverage the reflection from the input surface to directly visualize the intensity pattern of the input plane, as shown in figure 14(b). Note that for the later approach to be reliable, it is necessary to properly align the system to ensure that the plane of the input facet corresponds exactly to the Fourier plane of the DMD, and that the input facet plane is conjugated with the camera plane.

We hypothesize that the aberrations brought about by the DMD are smooth, and can be depicted by a phase pattern ϕ^{aber} in the plane of the DMD array. This could be feasibly approximated by a finite number of Zernike polynomials $Z_n(r,\theta)$ [29], as follows:

$$\phi^{\text{aberr}}(r,\theta) \approx \sum_{n=0}^{N} a_n Z_n(r,\theta)\,. \tag{6}$$

The goal is to find and display the phase value ϕ_i^{corr} on each macropixel i that best compensates for the aberrations, i.e. $\phi_i^{\text{corr}} = -\phi^{\text{aber}}(r_i,\theta_i)$. We create this pattern in the basis of Zernike polynomials

$$\phi_i^{\text{corr}} = \sum_{n=0}^{N} a'_n Z_n(r,\theta)\,, \tag{7}$$

the best correction is obtained for

$$a'_n = -a_n \;\forall n \in [0..N]\,. \tag{8}$$

We perform a sequential optimization of parameters a_n to maximize a specific function designed to be maximal for the ideal correction of optical aberrations. The approach is inspired by methods used for focusing through complex disordered media [1], by effectively treating the aberrations of the DMD as equivalent to propagation through an unknown linear medium. For each degree of freedom (i.e. the phase on one group of pixels in [1], or the coefficient of one Zernike polynomial in this section), we scan different values and retain the one that maximizes the intensity at the target location. We first generate a mask, represented by a disk, centered around the point of maximum intensity of the original image (refer to figure 13(d)) with a radius equivalent to a single speckle grain. The exact size of this radius for a successful optimization is not critical and can be determined by approximating the dimensions of the ideal PSF, expressed as $r_0 \approx M\frac{\lambda}{2NA}$, where NA is the numerical aperture of the optical system and M refers to its magnification. For a given output intensity pattern, we compute an element-wise product between this image and the created mask, followed by a summation. This calculated sum is then divided by an analogous product, but with the complementary mask substituted in place of the original in order to minimize the side lobes of the PSF. We set initial parameter values as $a'_n = 0\;\forall n \in [0..N]$. For each parameter, we test different values of a'_n, construct the phases for every micropixel according to $\phi_i^{\text{corr}} = \sum_{n=0}^{N} a'_n Z_n(r_i,\theta_i)$, record the resulting intensity profile, and evaluate the corresponding cost function. For each parameter, the value that results in the maximum output is retained. To mitigate potential noise or instability, this complete process is reiterated 3 times for each parameter.

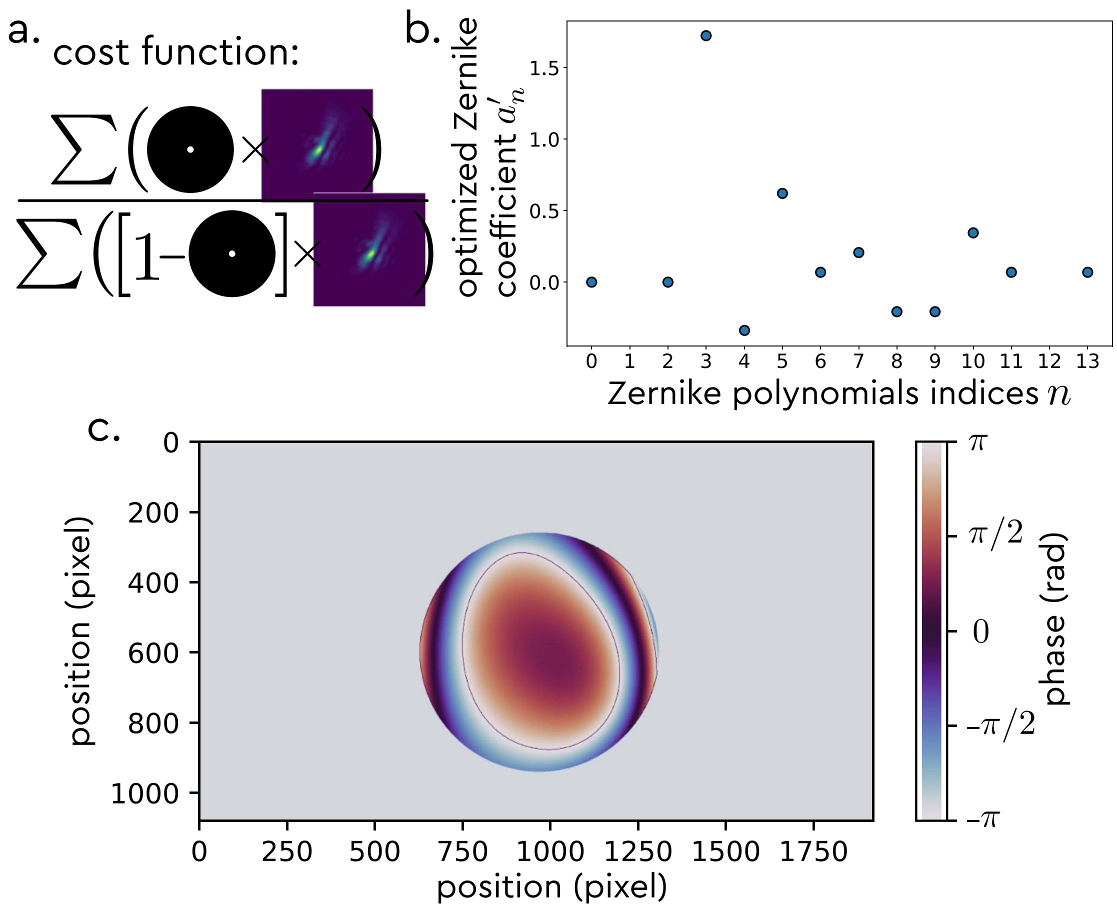

Figure 15. Correction phase map. (a) Schematic representation of the function we want to optimize, i.e. we optimize the ratio between the sum of the intensity of the measured image in a diffraction-limited disk and the sum of the intensity elsewhere. We both want to maximize the intensity of the main lobe of the PSF and minimize its side lobes. (b) Values of the experimentally obtained optimal coefficients in the Zernike polynomials basis. (c) Resulting optimal phase pattern in the chosen illumination area.

To estimate the quality of the correction, we compute the Strehl ratio of the PSF. It is defined as the maximum of the measured PSF divided by the maximum of the ideal one. This optimal PSF is the squared modulus of the Fourier transform of a circular aperture [30]:

$$PSF_{\mathrm{ideal}} \propto \left[J_1\left(ka\frac{R}{\sqrt{R^2+f^2}}\right)\right]^2, \tag{9}$$

with J_1 the Bessel function of the first kind of order 1, $k = 2\pi/\lambda$ the wavenumber, a the radius of the aperture, R the radial coordinate in the Fourier plane, and f the focal length of the lens.

As an illustration, we conduct an optimization procedure using 11 Zernike polynomials. We use a V-9501 Vialux DMD with a DLP9500 TI chip of resolution 1920 by 1200 pixels and a pixel pitch of 10.8 μm. The optimization is performed on a disk of radius 340 pixels, The illumination is done using an expanded laser beam at 633 nm, corresponding to the aperture of our optical setup. We exclude the first three Zernike polynomials in the optimization process, starting from the radial degree 2. Indeed, the initial one, known as the piston, does not influence the PSF quality. The subsequent ones, the tip and the tilt, cause the PSF to shift. Our procedure relies on optimizing the maximum of the PSF, wherever that is, rendering us indifferent to these two parameters. After optimization, it is possible to generate the correction pattern using a selected number of Zernike polynomials in order to investigate their impact on the PSF quality. We see here that using about 10 Zernike polynomials is sufficient to obtain a Strehl ratio > 0.99. Figure 16 demonstrates the Strehl ratio and the intensity profiles of the PSF for different counts of the utilized Zernike polynomials. It is important to note that we do not use the full surface of the DMD. Using a larger area may lead to stronger deformations of the PSF, requiring a larger number of Zernike polynomials to be corrected accurately. The experimental data, in addition to the Python code used to generate the figures, can be accessed in the dedicated repository [23].

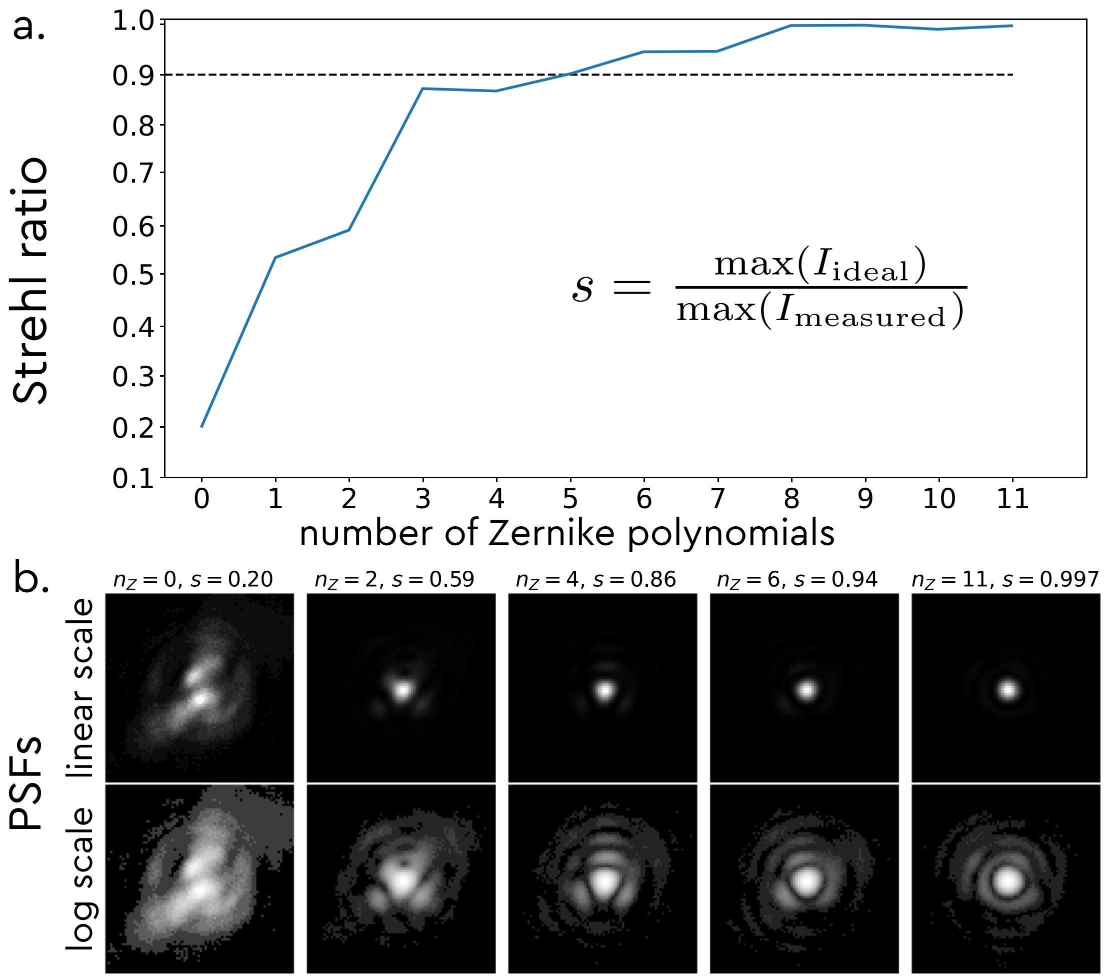

Figure 16. Effect of Zernike polynomials on the optimization of the PSF. (a) Strehl ratio of the PSF as a function of the number of Zernike polynomials used for the compensation of the aberrations. (b) Intensity profile of the PSF for different number of Zernike polynomials in linear and logarithmic scale. To generate this data, we take the final solution of the optimization experimental procedure, i.e. the optimal coefficients a'_n, and generate the corrected PSF with an increasing number of Zernike polynomials.

3.3. Python code example

We provide in the paper repository [23] a Python code example to simulate the effect of aberration on a DMD and then perform a sequential optimization as previously proposed to learn the characterize pattern. We make use of the !aotools! package [31] for generating Zernike polynomials.

TL;DR:
DMDs are not flat and can introduce aberrations; these are typically much stronger than those commonly observed with liquid crystal SLMs. This can be counteracted *in situ* using a standard setup and a straightforward optimization procedure to maximize the intensity at the central position of the PSF.

4. Mechanical and thermal stability

Unlike the original purpose of the DMD, i.e. amplitude modulation for video projectors, typical scientific applications require a high stability of the generated wavefront. This is particularly true for applications in complex media, such as strongly scattering media or multimode fiber, where a small change in the phase front can lead to a large change in the output intensity profile. While LC-SLMs design has been improved and adapted to scientific applications over the last decades, DMD are still relatively new tools for wavefront shaping and sensing and are prone to instabilities that need to be addressed by the user. In this section, we present the effect of mechanical and thermal instabilities and how to limit their impact on the wavefront quality with simple solutions.

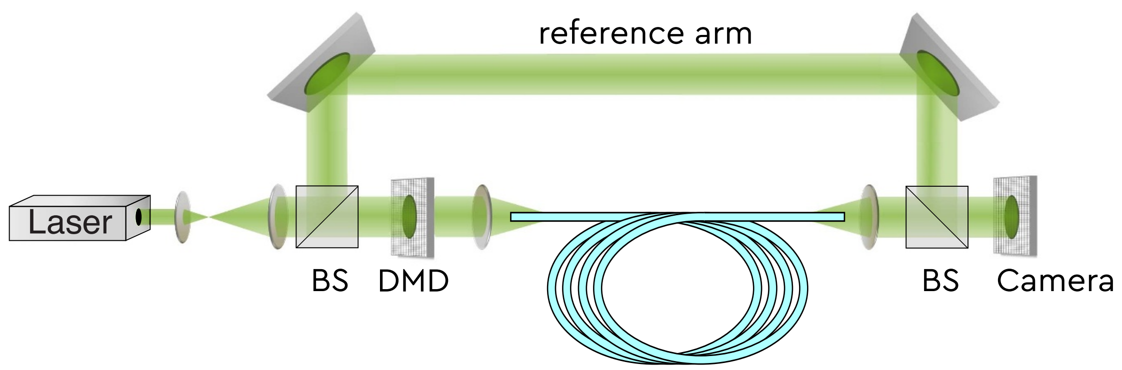

Figure 17. Measuring stability at the output of a multimode fiber. Schematic representation of the setup used to measure the phase fluctuations through a multimode fiber. An equivalent setup can be used with a scattering medium.

4.1. Mechanical stability

Most DMD kits consist of two primary components, the chip itself and the electronic board that controls it. This could be the standard electronics board typically used for video projectors, as seen in TI evaluation kits, or an FPGA specifically designed for rapid scientific usage, as offered by Vialux [8] for instance. Integral to these electronics is a fan designed to cool both the chip and the electronic board. However, due to the use of a rigid flat cable for connection between the chip and the electronics board, these parts are not mechanically independent. As such, vibrations originating from the board are partially transmitted to the chip, resulting in minute rotations of the mirror surface. Although this perturbation is inconsequential for video projection, they can have significant impacts on applications involving complex media given their high sensitivity to phase front variations.

Due to its high sensitivity in complex media, it is convenient to characterize this effect directly on the system's response, rather than constructing a distinct setup to analyze the wavefront itself. An example of such a setup is demonstrated in figure 17, although a similar approach can be employed with a scattering medium. We enlarge a laser beam onto the DMD and transmit the incoming light through a multimode fiber. Additional elements are required in the setup to fulfill the requirement for complex modulation [16]. For the sake of clarity, we present a simplified version of the setup where those elements are not present. The output from the fiber is then made to interfere with a reference arm in an off-axis configuration [32], allowing us to detect changes in the output complex field by recording the interference pattern using a camera.

In the supplementary materials [33], we present an animation illustrating the dynamic pattern. In off-axis holography, the local transverse displacement of the fringes is directly proportional to the phase, with a displacement equivalent to the period of the fringes corresponding to 2π [32]. This permits us to estimate the fluctuation in phase over time at a given position of the output plane. As illustrated in figure 18(depicted by the red curve), the phase varies rapidly over time, a fluctuation attributed to the rapid mechanical vibrations transmitted by the board.

A simple yet effective solution consists in damping the vibrations at the flat cable's level by clamping it with a soft material, as depicted in figure 19. This can be achieved using commonly available materials. In this context, we utilize simple foam, typically used for packaging, and secure it to the cable with two metallic plates, screws, and nuts. We observe a significant decrease in the phase fluctuations, as demonstrated in figure 18(blue curve).

TL;DR:
The functioning of DMDs can be perturbed by vibrations transmitted from the electronics board via the rigid flat cable that links it to the DMD chip. This adverse effect can be minimized by securing the cable with a soft material that serves to dampen these vibrations.

4.2. Thermal stability

Electronics utilized to control the DMD chip experience thermal variations during operation. The dynamics of this effect are dependent on the frame rate. Specifically, the chips heats up more quickly when increasing the frame rate. The increase of temperature can reach more than 15° Celsius when running a sequence at maximum speed (20–30 kHz) [34]. Notably, this effect is less pronounced when the device is on but not running a sequence. Temperature fluctuations can cause deformations on the chip's

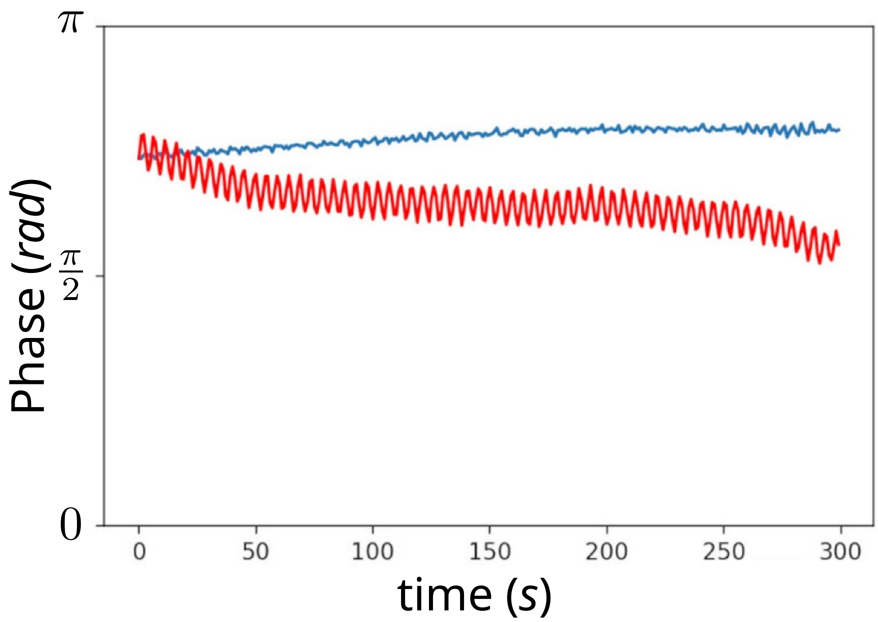

Figure 18. Vibration induced phase fluctuations. Phase fluctuations measured over time at a specific position on a plane located at the distal end of a multimode fiber. We employ off-axis holography using the setup depicted in figure 17. The red and blue curves correspond to the phase fluctuations measured respectively without and with vibration damping by securing the flat cable with foam, as illustrated in figure 19.

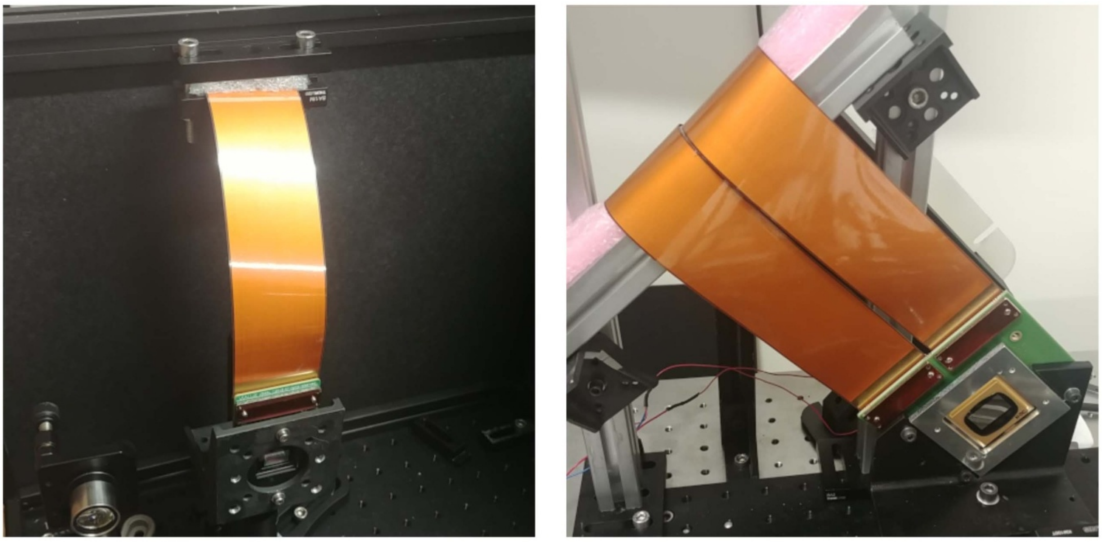

Figure 19. Damping mechanical vibrations. Pictures of experimental setups where a damping of the vibrations is implemented. (a) The flat cable is secured with foam and metallic plates. (b) The flat cable is in tension against a foam material supported by a metallic plate.

surface and can modify the phase response of the glass protective window. This creates low order aberrations, which degrade the quality of the wavefront. While this issue is comparatively less critical than static aberrations and mechanical instabilities previously detailed, it nonetheless has a substantial impact on the complex medium's response when a DMD is employed to modulate the input wavefront.

Empirically, we observe deformations of the pattern at the output of the medium under study when the DMD chip heats up after switching on the device. These deformations originate from a temperature-dependent perturbation of the modulated field. We attribute this effect to the transparent part of the DMD (i.e. the protection glass window) having a refractive index that significantly changes with temperature. Once the device reaches thermal equilibrium, this effect stabilizes, allowing us to find the appropriate correction mask as described in section 3 of the manuscript. It is important to stress that it is the

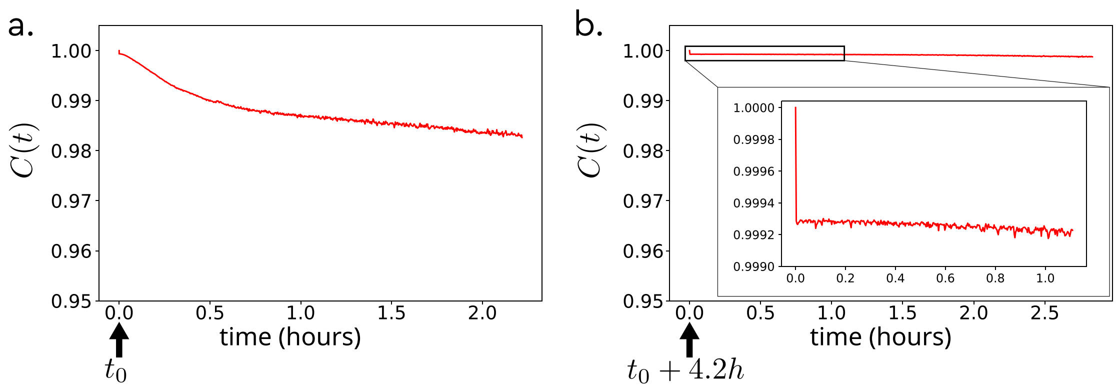

Figure 20. Effect of temperature. Temporal decorrelation of a speckle pattern measured at the output of a multimode fiber when running a sequence in an infinite loop. We use equation (10) to estimate the correlation between the intensity pattern at a given time t and the one at $t = 0$. $t = 0$ corresponds respectively to the start of the sequence (a) and to 4.2 h after the start of the sequence (b).

thermal fluctuations that impact the stability of the modulation, not the temperature itself, as we obtain stable experimental conditions even when equilibrium is reached at the maximal operating temperature of the modulator without thermal cooling.

Before initiating a wavefront shaping experiment, it is important to characterize the influence of temperature to assess the extent to which it impacts the results. Although the exact effect on the wavefront distortion can be directly quantified [34], it is typically more convenient to directly measure the effect on the studied system's response. Directly using the output of the complex medium under study presents multiple advantages. First, it allows the setup to remain unchanged and facilitates easy re-characterization of the effect if some parameters change. Additionally, complex media tend to be very sensitive to input phase changes, with the sensitivity varying from one medium to another. By using the complex medium itself, we obtain the exact sensitivity needed for the current setup. Therefore, regardless of the qualitative changes in the input field, stability in the output indicates that the setup is adequate for studying the medium in question. To do so, we use a setup similar to the one presented in the previous section and depicted in figure 17. We can then estimate the field or intensity decorrelation over time. We present here results with intensity correlation, as it does not require a reference arm. The measured output pattern typically take the form of a seemingly random speckle pattern, that is sensitive to minute changes in the input wavefront. The correlation estimation is obtained by comparing the output intensity pattern $I(\vec{r},t)$ at a given time t to the one at $t = 0$. We use the following expression for the correlation:

$$C(t) = \frac{\langle \bar{I}(\vec{r},t)\bar{I}(\vec{r},t=0)\rangle_{\vec{r}}}{\sqrt{\left\langle \bar{I}(\vec{r},t)^2\right\rangle_{\vec{r}}\left\langle \bar{I}(\vec{r},t=0)^2\right\rangle_{\vec{r}}}}, \quad (10)$$

with $\bar{I}(\vec{r},t) = I(\vec{r},t) - \langle I(\vec{r},t)\rangle_t$ and $\langle . \rangle_{\vec{r}}$. $\langle . \rangle_t$ represent the spatial averaging over the region of interest of the output plane (i.e. the plane of the camera sensor) and the temporal averaging over the measured frames. Figure 20 shows the measured decorrelation over time when running an sequence in an infinite loop. $t = 0$ correspond in the first case (a) to the start of a sequence and in the second case (b) is set to 4.2 h after the start of the sequence. For the scenario (a), it is worth noting that before the sequence commenced, the DMD was active but remained in the idle state, meaning that it was not executing a sequence. We observe a non-negligible decorrelation over time after the sequence started that slows down after about 1 h h after starting the sequence, the correlation is now stable.

The more efficient way to counteract this effect is to use a closed-loop system to stabilize the temperature of the DMD chip. This can be achieved by using a thermoelectric cooler as demonstrated in [34] and depicted in figure 21.

TL;DR:
DMDs take about an hour to thermally stabilize when a sequence is running. It can be countered by using a thermoelectric cooler and a temperature sensor. It can also be simply mitigated by letting a sequence run for few hours before starting the experiment.

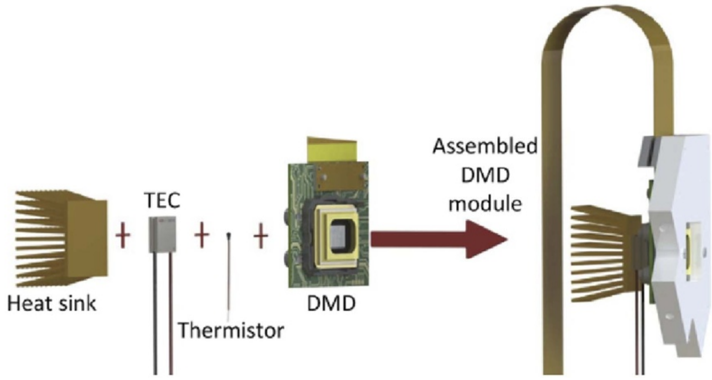

Figure 21. Thermal stabilization of the DMD chip. Schematic representation of the setup utilized to regulate the temperature of the DMD chip. A thermoelectric cooler and a heat sink is employed to control the temperature, while a thermistor is used to measure deviations from the temperature setpoint. A closed-loop system is used to regulate the temperature. Reproduced from [34].

5. Conclusion

DMDs are powerful tools for wavefront shaping applications in complex media due to their high pixel count, relative low cost, and high refresh rate. However, mostly due to their original purpose of amplitude modulation of incoherent light for video projection, several effects need to be taken into account when using DMDs for wavefront shaping. First, the choice of its pixel pitch must be made carefully by considering the wavelength of operation to ensure a good modulation quality and diffraction efficiency. Furthermore, the DMD surface is not flat and can introduce aberrations which can be corrected using a simple optimization procedure. Finally, the DMD is sensitive to mechanical vibrations and thermal variations, which can be mitigated ensuring a good mechanical and thermal isolation of the device.

Acknowledgments

S M P, M W M, and R G C acknowledge the French *Agence Nationale pour la Recherche* Grants No. ANR-23-CE42-0010-01 MUFFIN and ANR-20-CE24-0016 MUPHTA and the Labex WIFI Grants No. ANR-10-LABX-24, ANR-10-IDEX-0001-02 PSL*. L M, J C, M G, and R G acknowledge Cathie Ventalon for sharing a V-module and for her valuable discussions. L M, J C, M G, and R G were funded by Centre National de la Recherche Scientifique MITI/80Prime and the iXcore—iXlife—iXblue Fundation.

Data availability statement

The data that support the findings of this study are openly available at the following URL/DOI: https://github.com/wavefrontshaping/tutorial-DMD-setup-2023 [35].

Data and code availability

Data and code examples are available in the dedicated repository [23].

Author contributions

Sébastien M Popoff 0000-0002-7199-9814
Conceptualization (equal), Data curation (equal), Formal analysis (equal), Investigation (equal), Methodology (equal), Project administration (equal), Software (equal), Supervision (equal), Validation (equal), Visualization (equal), Writing – original draft (equal), Writing – review & editing (equal)

Louis Malosse 0009-0004-9006-9374
Data curation (equal), Formal analysis (equal), Funding acquisition (equal), Investigation (equal), Resources (equal), Validation (equal), Visualization (equal), Writing – review & editing (equal)

Rodrigo Gutiérrez-Cuevas 0000-0002-3451-6684
Conceptualization (equal), Investigation (equal), Methodology (equal), Project administration (equal), Validation (equal), Writing – review & editing (equal)

Yaron Bromberg 0000-0003-2565-7394
Conceptualization (equal), Methodology (equal), Validation (equal), Writing – review & editing (equal)

Jean Commère 0009-0000-4710-4972
Investigation (equal), Supervision (equal), Validation (equal), Visualization (equal), Writing – review & editing (equal)

Marie Glanc
Investigation (equal), Supervision (equal), Validation (equal), Writing – review & editing (equal)

Raphaël Galicher 0009-0007-9980-5966
Investigation (equal), Supervision (equal), Validation (equal), Writing – review & editing (equal)

Appendix A. 1D calculation of the DMD diffraction effect

Assuming the effect of the device's finite size and illumination to be negligible, we can represent the field reflected from the device under the influence of plane wave illumination across two systems as follows. Here, θ_B denotes the blaze angle, i.e. the tilt of the micromirror normal with respect to the device normal, so that the corresponding specular direction is $2\theta_B - \alpha$:

$$\begin{aligned} R_{\text{flat}}(x) &\propto \left[\Pi(x/d') \otimes_x \sum_k \delta(x-kd)\right] e^{j\frac{2\pi}{\lambda}\sin(\alpha)x}, \\ R_{\text{blazed}}(x) &\propto \underbrace{\left(\underbrace{\Pi(x/d')}_{\text{pixel size}} \underbrace{e^{j\frac{2\pi}{\lambda}(\sin(2\theta_B-\alpha)-\sin(\alpha))x}}_{\substack{\text{blazed angle ,}\\ \text{+ angle of incidence}}}\right)}_{\text{pixel response}} \otimes_x \underbrace{\sum_k \delta(x-kd)}_{\text{periodicity}} e^{j\frac{2\pi}{\lambda}\sin(\alpha)x}. \end{aligned} \tag{11}$$

with $\Pi(x)$ the rectangular function, representing the finite size of the pixel, defined as:

$$\Pi(x) = \begin{cases} 1, & \text{if } -\frac{1}{2} < x < \frac{1}{2}, \\ 0, & \text{otherwise.} \end{cases} \tag{12}$$

The filling fraction, in the 1D case, is the ratio of the size of the pixels (or micro-mirrors) d', and the pitch d, such that $d' = \rho d$.

The Fourier transform of equation (11) can be written as:

$$\begin{aligned} I_{\text{flat}}(\theta) &\propto \sum_p \delta(\sin(\theta)+\sin(\alpha)-p\sin(\theta_D)) \times \text{sinc}^2\left(\pi\rho\frac{\sin(\theta)-\sin(\alpha)}{\sin(\theta_D)}\right) \\ I_{\text{blazed}}(\theta) &\propto \underbrace{\sum_p \delta(\sin(\theta)+\sin(\alpha)-p\sin(\theta_D))}_{\text{orders of diffraction}} \times \underbrace{\text{sinc}^2\left(\pi\rho\frac{\sin(\theta)-\sin(2\theta_B-\alpha)}{\sin(\theta_D)}\right)}_{\text{envelope}}. \end{aligned} \tag{13}$$

We observe that the envelope (right-hand term) is maximal for $\sin(\theta_{\text{max}}) = \sin(2\theta_B - \alpha)$, while the effect of the periodicity (left-hand term) is maximal when $\sin(\theta_p) + \sin(\alpha) = p\lambda/d$, representing the orders of diffraction.

Appendix B. 2D calculation of blazed grating condition

To analyze more precisely the effect of diffraction in a DMD, one needs to consider the 2D surface of the modulator. We can establish a Cartesian coordinate system on the plane of the DMD, with axes x

and y aligned with the pixel sides (refer to figure 5(a). The pixels are uniformly repeated along these axes. However, a technical challenge arises in that the axis of rotation of the pixels aligns with the pixel diagonals, resulting in a rotation by 45° with respect to the x and y axes. For the convenience of alignment and manipulation of the optical setup, it is preferable to work with the incident and outgoing beams which have the optical axis contained in the horizontal plane, i.e. a plane parallel to the table surface. A straightforward and common solution is to rotate the chip by 45° relative to the horizontal plane, which aligns the pixel axis of rotation to be vertical.

A more detailed description of the 2D system and computation of its response can be found in [12]. However, we can find a simple condition for having most of the energy in one diffraction order by looking at the effect of the tilts of the mirrors when the axis is rotated by 45° compared to the axis of the pixel array (axes x and y). We consider a plane wave with an incoming angle α contained in the horizontal plane (i.e. orthogonal to the rotation axis of the micro-mirrors). The effect of this angle is represented by a phase term of the form:

$$\vec{k}_{\text{in}} \cdot \vec{r} = \frac{2\pi}{\lambda} \sin\alpha \frac{(x-y)}{\sqrt{2}}, \tag{14}$$

with $\vec{k}_{\text{in}}$ the incoming wavevector and $\vec{r}$ the position in the modulator plane, represented by the coordinate (x, y).

The grating condition is achieved when the output contributions are in phase for the output angle corresponding to the specular reflection on the tilted mirrors. It corresponds to the plot on the left in figure 4 for the 1D case. The phase contribution resulting from an output angle $2\theta_B - \alpha$, corresponding to the specular reflection on each micro-mirror, reads:

$$\vec{k}_{\text{out}} \cdot \vec{r} = \frac{2\pi}{\lambda} \sin(2\theta_B - \alpha) \frac{(x-y)}{\sqrt{2}}. \tag{15}$$

The total phase then reads:

$$\phi(x,y) = \vec{k}_{\text{in}}.\vec{r} + \vec{k}_{\text{out}}.\vec{r} = \frac{2\pi}{\lambda} \sin(2\theta - \alpha) \frac{(x-y)}{\sqrt{2}} + \frac{2\pi}{\lambda} \sin\alpha \frac{(x-y)}{\sqrt{2}}. \tag{16}$$

We see that x and y have the same effect. The grating condition is then achieved when two consecutive pixels, separated by a distance d in both the x and y directions, are in phase. I.e. for

$$\phi(x,y) = \phi(x+d,y) = \phi(x,y+d). \tag{17}$$

The new blazed grating equation then reads :

$$\sin(2\theta_B - \alpha) + \sin(\alpha) = 2\sin(\theta_B)\cos(\theta_B - \alpha) = p\frac{\sqrt{2}\lambda}{d}, \tag{18}$$

References

[1] Vellekoop I M and Mosk A P 2007 Focusing coherent light through opaque strongly scattering media *Opt. Lett.* **32** 2309

[2] Cha S, Lin P C, Zhu L, Sun P-C and Fainman Y 2000 Nontranslational three-dimensional profilometry by chromatic confocal microscopy with dynamically configurable micromirror scanning *Appl. Opt.* **39** 2605–13

[3] Zhuang Z and Ho H P 2020 Application of digital micromirror devices (DMD) in biomedical instruments *J. Innovat. Opt. Health Sci.* **13** 2030011

[4] Yoon T, Kim C-S, Kim K and Choi J-r 2018 Emerging applications of digital micromirror devices in biophotonic fields *Opt. Laser Technol.* **104** 17–25

[5] Gauthier G, Lenton I, Parry N M, Baker M, Davis M J, Rubinsztein-Dunlop H and Neely T W 2016 Direct imaging of a digital-micromirror device for configurable microscopic optical potentials *Optica* **3** 1136–43

[6] Hornbeck L J 1997 Digital light processing for high-brightness high-resolution applications *Proc. SPIE* **3013** 27–40

[7] Dudley D, Duncan W M and Slaughter J 2003 Emerging digital micromirror device (DMD) applications *Proc. SPIE* **1** 14–25

[8] ViALUX Messtechnik and Bildverarbeitung GmbH 2023 Home vialux gmbh (available at: https://www.vialux.de/en/index.html) (Accessed 23 January 2023)

[9] Hofling R and Ahl E 2004 ALP: universal DMD controller for metrology and testing *Proc. SPIE* **5289** 322–9

[10] Cox M A and Drozdov A V 2021 Converting a Texas instruments DLP4710 DLP evaluation module into a spatial light modulator *Appl. Opt.* **60** 465

[11] Park M-C, Lee B-R, Son J-Y and Chernyshov O 2015 Properties of DMDs for holographic displays *J. Mod. Opt.* **62** 1600–7

[12] Scholes S, Kara R, Pinnell J, Rodríguez-Fajardo V and Forbes A 2019 Structured light with digital micromirror devices: a guide to best practice *Opt. Eng., Bellingham* **59** 1

[13] Wang X and Zhang H 2023 Diffraction characteristics of a digital micromirror device for computer holography based on an accurate three-dimensional phase model *Photonics* **10** 130

[14] Popoff S M, Lerosey G, Carminati R, Fink M, Boccara A C and Gigan S 2010 Measuring the transmission matrix in optics: An approach to the study and control of light propagation in disordered media *Phys. Rev. Lett.* **104**

[15] Lee W-H 1979 Binary computer-generated holograms *Appl. Opt.* **18** 3661

[16] Gutiérrez-Cuevas R and Popoff S M 2023 Binary holograms for shaping light with digital micromirror devices *J. Phys. Photonics* **6** 045022

[17] Jackson J D 2019 Visual analysis of a Texas instruments digital micromirror device (available at: www2.optics.rochester.edu/workgroups/cml/opt307/spr05/john/) (Accessed 18 September 2021)

[18] Texas instruments DLP display and projection chipset selection guide Texas Instruments (available at: https://www.ti.com/lit/sg/sprt736d/sprt736d.pdf) (Accessed 18 September 2021)

[19] Casini R and Nelson P G 2014 On the intensity distribution function of blazed reflective diffraction gratings *J. Opt. Soc. Am. A* **31** 2179

[20] Popoff S M Setting up a DMD: Diffraction effects (available at: https://www.wavefrontshaping.net/post/id/21) (Accessed 18 November 2023)

[21] Goorden S A, Bertolotti J and Mosk A P 2014 Superpixel-based spatial amplitude and phase modulation using a digital micromirror device *Opt. Express* **22** 17999

[22] Popoff S M DMD diffraction tool (available at: https://www.wavefrontshaping.net/post/id/49) (Accessed11 September 2023)

[23] Popoff S M and Gutiérrez-Cuevas R 2023 Repository for the paper "a practical guide to digital micro-mirror devices (DMDs) for wavefront shaping (available at: https://github.com/wavefrontshaping/tutorial-DMD-setup-2023) (Accessed 1 January 2026)

[24] Wei G, Bhushan B and Jacobs S J 2004 Nanomechanical characterization of multilayered thin film structures for digital micromirror devices *Ultramicroscopy* **100** 375–89

[25] Cao K, Liu W and Talghader J J 2001 Curvature compensation in micromirrors with high-reflectivity optical coatings *J. Microelectromech. Syst.* **10** 409–17

[26] Brown P T, Kruithoff R, Seedorf G J and Shepherd D P 2021 Multicolor structured illumination microscopy and quantitative control of polychromatic light with a digital micromirror device *Biomed. Opt. Express* **12** 3700

[27] Matthès M W, del Hougne P, de Rosny J, Lerosey G and Popoff S M 2019 Optical complex media as universal reconfigurable linear operators *Optica* **6** 465–72

[28] Lee B-R, Marichal-Hern'andez J G, Rodriguez-Ramos J M, Venkel T and Son J-Y 2023 Compensation of wavefront aberration introduced by DMDs' operation principle *Opt. Mater.* **140** 113863

[29] von F Zernike 1934 Beugungstheorie des schneidenver-fahrens und seiner verbesserten form, der phasenkontrastmethode *Physica* **1** 689–704

[30] Airy G B 1835 On the diffraction of an object-glass with circular aperture *Trans. Cam. Phil. Soc.* **5** 283

[31] Townson M J, Farley O J D, de Xivry G O, Osborn J and Reeves A P 2019 AOtools: a python package for adaptive optics modelling and analysis *Opt. Express* **27** 31316

[32] Cuche E, Marquet P and Depeursinge C 2000 Spatial filtering for zero-order and twin-image elimination in digital off-axis holography *Appl. Opt.* **39** 4070

[33] Popoff S M, Matthès M W, Bromberg Y and Gutiérrez-Cuevas R 2023 Supplementary material for 'A practical guide to Digital Micro-mirror Devices (DMDs) for wavefront shaping (available at: https://github.com/wavefrontshaping/tutorial-DMD-setup-2023) (Accessed 1 January 2026)

[34] Rudolf B, Du Y, Turtaev S, Leite I T and Čižm'ar T 2021 Thermal stability of wavefront shaping using a DMD as a spatial light modulator *Opt. Express* **29** 41808

[35] Available at: https://github.com/wavefrontshaping/tutorial-DMD-setup-2023.